Stability of Hexagons in Rotating non-Boussinesq Convection

Vadim Moroz+, Werner Pesch*, Hermann Riecke+
+*Department of Engineering Sciences and Applied Mathematics,*
Northwestern University, 2145 Sheridan Rd, Evanston, IL, 60208, USA,
**Theoretische Physik II, Universität Bayreuth, D-95440 Bayreuth, Germany*

(Dated: July 2, 2002)

Motivated by the impact of rotation on the stability of convection roll patterns, we investigate the stability of hexagon patterns in non-Boussinesq rotating convection for several experimentally relevant fluid systems and its dependence on the Rayleigh number, the wavenumber, and the rotation rate. In the weakly nonlinear regime the coefficients of the appropriate coupled Ginzburg-Landau equations are derived. Further above threshold a fully nonlinear Galerkin approach is employed to compute the hexagon and roll solutions and to perform their general linear stability analysis. Long- and shortwave instabilities, both steady and oscillatory, are identified. For small Prandtl numbers the band of stable hexagon solutions becomes very asymmetric in the wavenumber and oscillatory sideband instabilities are found already very close to onset.

PACS numbers: 47.20.Bp,47.54.+r,47.20.Ky,47.27.Te

I. INTRODUCTION

Rayleigh-Bénard convection, the convection instability of a fluid layer subject to a temperature gradient, has proven to be a rich system exhibiting various types of complex pattern-formation phenomena (for a recent review see [1]). Of particular current interest has been the spatio-temporal chaos found in rotating convection [2–4] that arises due to the Küppers-Lortz instability [5], and the spiral-defect chaos observed in non-rotating convection at small Prandtl numbers [6–11], which is driven by mean flow. In these states the disordered patterns are always of roll-type. For chaotic states based on other planforms like hexagons or squares, considerably less experimental data are available [12, 13].

Recently the stability of hexagon patterns in systems with broken chiral symmetry (e.g. due to rotation) has been investigated using coupled Ginzburg-Landau equations in the weakly nonlinear regime [14–16], as well as Swift-Hohenberg type equations [17] and a longwave order-parameter equation [18]. It was found that although there is always a wavenumber band of stable hexagons near onset, sideband instabilities can induce a transition to separate attractors that exhibit persistent spatio-temporal chaos. Within the Swift-Hohenberg and the longwave equation the stability balloon can close further above onset leading again to spatio-temporal chaos.

In the presence of rotation, the instability of the hexagons to rolls [19] *via* a mixed mode is replaced by a Hopf bifurcation to oscillating hexagons [20, 21]. Within the framework of the Ginzburg-Landau equations the oscillating hexagons are linearly stable but nonlinearly unstable to the formation of spiral defects [15], which then exhibit chaotic dynamics described by a single complex Ginzburg-Landau equation [22].

In experiments, hexagonal convection patterns are obtained in surface-tension-driven Marangoni convection (e.g. [23, 24]) and in buoyancy-driven non-Boussinesq convection (e.g. [25, 26]). In these systems deformations of the periodic patterns drive a mean flow. It becomes increasingly important in fluids with small Prandtl number and provides a non-local coupling of the convection modes [27–29]. To describe this coupling the usual coupled Ginzburg-Landau equations have recently been extended [30]. In the absence of mean flow only a transverse longwave phase mode is relevant in limiting the stable wavenumber band in the weakly nonlinear regime [31]. It leads to a shearing of the hexagon patterns since its modulation wavevector is perpendicular to the translation induced by the phase modulation. For sufficiently small Prandtl numbers, however, the longitudinal phase mode, which leads to compressions and expansions of the hexagons, is expected to be relevant as well and to lead to qualitatively different transients in the relaxation from unstable to stable hexagon patterns [30]. Preliminary investigations indicate that in the presence of rotation mean flow can induce a transition to a spatio-temporally chaotic state characterized by the proliferation of penta-hepta defects [32].

No quantitative results have been available so far for the stability of hexagonal patterns in rotating non-Boussinesq convection. In this paper we address this problem from two directions. We first derive the coefficients for the weakly nonlinear coupled Ginzburg-Landau equations, which are valid in the weakly non-Boussinesq regime when the fluid parameters vary only slightly with temperature. They provide quantitative predictions for the stability of hexagons with respect to sideband perturbations as well as the domain of existence of oscillating hexagons. Then we use a fully nonlinear Galerkin method to determine the general stability of hexagons and rolls for realistic set-ups using water and CO_2 as fluids. Of particular interest are the shortwave and the oscillatory sideband instabilities that arise in the rotating system. If the new laser heating technique that allows the printing of (almost) arbitrary planforms as initial conditions in Bénard-Marangoni convection [24] can be applied to buoyancy-driven convection with rotation, experimental investigations of these instabilities will be very interesting, since various simulations of model systems suggest the possibility of persistent time-periodic or chaotic dynamics [14, 17, 32]. In the strongly non-Boussinesq case, in which hexagons persist up to relatively large values of the control parameter, we find that for small wavenumbers certain resonant mode interactions have a strong effect on the hexagon patterns and their stability limits.

The paper is organized as follows. In sec.II we state the basic convection equations. Sec.III is dedicated to the coefficients for the weakly nonlinear Ginzburg-Landau equations. In sec.IV we discuss the resulting stability properties of hexagons. The results of a fully nonlinear stability analysis of hexagons with rotation are presented in sec.V.

II. BASIC EQUATIONS

We consider convection in a horizontal liquid layer of thickness d, heated from below (at temperature T_1) and cooled from above (at temperature $T_2 < T_1$), which is rotated about a vertical axis with angular velocity $\omega\vec{\mathbf{k}}$. It is described by the Navier-Stokes equations

$$\begin{aligned}\partial_t(\rho u_i) + \rho u_j \partial_j u_i &= -\partial_i p - \rho g \delta_{i3} + \partial_j \left(\nu\rho(\partial_i u_j + \partial_j u_i) + \bar{\nu}\rho\delta_{ij}\partial_k u_k\right) + \\ &\quad + 2\rho\omega\epsilon_{ijk} r_i u_j \delta_{k3} + \frac{1}{2}\rho\omega^2\partial_i(x^2+y^2), \qquad (1)\end{aligned}$$

the continuity equation

$$\partial_t\rho + \partial_j(\rho u_j) = 0, \qquad (2)$$

and the heat equation

$$\partial_t T + u_j\partial_j T = \frac{1}{\rho c_p}\partial_j(\lambda\partial_j T) - \frac{p}{\rho c_p}\partial_j u_j + \frac{1}{\rho c_p}\Phi. \qquad (3)$$

Here $\vec{u} = (u_1, u_2, u_3)$ is the fluid velocity, T the temperature, ρ the density of the fluid, p the pressure, g the acceleration of gravity, ν the viscosity, $\bar{\nu}$ the volume viscosity, Φ the viscous heating (cf. (4)), and c_p the specific heat of the fluid. The orthogonal coordinates are chosen so that the z-axis is directed vertically upwards. The radius vector $\vec{r} = (x, y, z)$ is measured from some point on the axis of rotation, $\vec{\mathbf{k}}$ is the unit vector in the z-direction, δ_{ij} is the Kronecker delta, and ϵ_{ijk} is the unit antisymmetric tensor of the third rank. The Einstein convention of summation over repeated indices is assumed. The viscous heating Φ in the heat equation (3) is given by

$$\Phi = \nu\rho\left(2e_{ij}e_{ij} - \frac{2}{3}(e_{jj})^2\right) \qquad (4)$$

with $e_{ij} = \frac{1}{2}(\partial_j u_i + \partial_i u_j)$ being the stress tensor.

Realistic rigid boundary conditions are taken at the top and bottom plates, which are assumed to be kept at fixed temperatures $T_0 \pm \Delta T/2$:

$$\begin{aligned}\vec{u} &= 0 \text{ at } z = \pm\frac{d}{2}, &(5)\\ T &= T_0 + \frac{\Delta T}{2} \text{ at } z = -\frac{d}{2}, &(6)\\ T &= T_0 - \frac{\Delta T}{2} \text{ at } z = +\frac{d}{2}. &(7)\end{aligned}$$

Here $T_0 = (T_1 + T_2)/2$ denotes the mean temperature and $\Delta T = (T_1 - T_2) > 0$ the temperature difference between $z = \mp d/2$.

Since we focus in this paper on weakly non-Boussinesq convection we keep the temperature dependence of the various fluid properties to leading order. In our treatment we closely follow the formulation of the problem in [19]. For typical fluids the ratio $\frac{\alpha g d}{c_p}$ (with α the thermal expansion coefficient) is very small. For water it is approximately equal to $5 \cdot 10^{-8}$, for oil and air it is approximately $3 \cdot 10^{-7}$. In the heat equation this allows us to neglect the compressibility term proportional to p as well as the viscous heating Φ. In addition, in this parameter regime the pressure dependence of the fluid parameters is much weaker than their temperature dependence. We therefore neglect the pressure dependence. We write the Taylor expansion about the mean temperature T_0 in the form [19]

$$\frac{\rho(T)}{\rho_0} = 1 - \gamma_0 \frac{T - T_0}{\Delta T}(1 + \gamma_1 \frac{T - T_0}{\Delta T}) + ... \tag{8}$$

$$\frac{\nu(T)}{\nu_0} = 1 + \gamma_2 \frac{T - T_0}{\Delta T} + ... \tag{9}$$

$$\frac{\lambda(T)}{\lambda_0} = 1 + \gamma_3 \frac{T - T_0}{\Delta T} + ... \tag{10}$$

$$\frac{c_p(T)}{c_{p0}} = 1 + \gamma_4 \frac{T - T_0}{\Delta T} + ... \tag{11}$$

where ρ_0, ν_0, λ_0, and c_{p0} denote the values of the respective quantities at the mean temperature T_0. The dots denote higher-order terms to be neglected in the sequel. In line with a clever experimental strategy we assume that T_0 is kept fixed when changing the main control parameter ΔT. Thus, the quantities $\gamma_i/\Delta T, i = 0, 2, 3, 4$, which describe, respectively, the slope of the density, viscosity, heat conductivity, and heat capacity at T_0 are fixed as well. The usual heat expansion coefficient at $T = T_0$ is, for instance, given by $\alpha_0 = \gamma_0/\Delta T$. Going beyond the Boussinesq approximation also the curvature of $\rho(T)$ at T_0 which is proportional to $\gamma_0\gamma_1/\Delta T^2$ comes into play. Note that the γ_i themselves, which give the relative change of the respective physical quantity across the layer, depend linearly on ΔT and thus on the Rayleigh number R (see below).

For constant fluid parameters the volume viscosity term $\bar{\nu}\rho\delta_{ij}\partial_k u_k$ and the centrifugal force $\frac{1}{2}\rho\omega^2\partial_i(x^2+y^2)$ can be absorbed into the pressure term. This is not true for the contributions from the temperature-dependent parts of $\bar{\nu}$ and ρ. While the z-dependence of the volume viscosity generates only a higher-order correction, neglecting the centrifugal force is only possible as long as the rotation rates are not too large, i.e. as long as $\gamma_0 L\omega^2/g$ is small. Here L is a characteristic measure of the horizontal system size.

For the non-dimensionalization it is convenient to introduce the heat diffusivity $\kappa_0 = \lambda_0/\rho_0 c_{p0}$, the dimensionless rotation rate $\Omega = 2\omega d^2/\nu_0$, the Prandtl number $Pr = \nu_0/\kappa_0$ and the Rayleigh number $R = \alpha_0 \Delta T g d^3/\nu_0\kappa_0$. We rescale the variables using the following units: length d, time d^2/κ_0, velocity κ_0/d, pressure $\nu_0\kappa_0\rho_0/d^2$, temperature $\nu_0\kappa_0/\alpha_0 g d^3 \equiv \Delta T/R$. We also introduce the dimensionless rescaled pressure $\tilde{p} = \nu_0\kappa_0\rho_0/d^2\,(p - \bar{\nu}\rho\partial_k(v_k\rho_0\kappa_0/\rho d))$ and rewrite the equations in terms of the dimensionless momenta $v_i = \rho d u_i/\rho_0\kappa_0$ instead of the velocities. With all of the above approximations the dimensionless equations are given by

$$Pr^{-1}(\partial_t v_i + \frac{v_j}{\rho}\partial_j v_i) = -\partial_i \tilde{p} - \frac{g d^3}{\nu_0 \kappa_0}\rho\delta_{i3} + \partial_j[\nu\rho(\partial_i(\frac{v_j}{\rho}) + \partial_j(\frac{v_i}{\rho}))] + \Omega\epsilon_{ijk}v_j\delta_{k3}, \tag{12}$$

$$\partial_t \rho + \partial_j v_j = 0, \tag{13}$$

$$\partial_t T + \frac{v_j}{\rho}\partial_j T = \frac{1}{\rho c_p}\partial_j(\lambda\partial_j T). \tag{14}$$

The conduction solution ($\vec{v} = 0$) of (12)-(14) is given by

$$T_{cond} = T_0 + R\left(-z - \frac{\gamma_3}{2}(z^2 - \frac{1}{4}) + \mathcal{O}(\gamma_3^2)\right). \tag{15}$$

We rewrite the temperature T in terms of the deviation Θ from the conductive profile (15) neglecting its contribution of $\mathcal{O}(\gamma_3^2)$,

$$\Theta = T - T_{cond} = T - T_0 - R\left(-z - \frac{\gamma_3}{2}(z^2 - \frac{1}{4})\right), \tag{16}$$

and obtain as final dimensionless equations

$$\begin{aligned}
\frac{1}{Pr}(\partial_t v_i + \frac{v_j}{\rho}\partial_j v_i) &= -\partial_i \tilde{p} + \delta_{i3}\left(1+\gamma_1(-2z+\frac{\Theta}{R})\right)\Theta + \\
&\quad +\partial_j\left[\nu\rho\left(\partial_i(\frac{v_j}{\rho})+\partial_j(\frac{v_i}{\rho})\right)\right] + \Omega\epsilon_{ijk}v_j\delta_{k3}, \qquad (17)\\
\partial_t\rho + \partial_j v_j &= 0, \qquad (18)\\
\partial_t\Theta + \frac{v_j}{\rho}\partial_j\Theta + R\frac{v_z}{\rho}(1+\gamma_3 z) &= \frac{1}{\rho c_p}\partial_j(\lambda\partial_j\Theta) - \gamma_3\partial_z\Theta. \qquad (19)
\end{aligned}$$

The dimensionless boundary conditions are

$$\vec{v}(x,y,z,t) = \Theta(x,y,z,t) = 0 \text{ at } z = \pm\frac{1}{2}. \qquad (20)$$

The nondimensionalized fluid parameters (8)-(11) read now:

$$\begin{aligned}
\rho(\Theta) &= 1-\gamma_0(-z+\frac{\Theta}{R}), \qquad (21)\\
\nu(\Theta) &= 1+\gamma_2(-z+\frac{\Theta}{R}), \qquad (22)\\
\lambda(\Theta) &= 1+\gamma_3(-z+\frac{\Theta}{R}), \qquad (23)\\
c_p(\Theta) &= 1+\gamma_4(-z+\frac{\Theta}{R}). \qquad (24)
\end{aligned}$$

We consider the non-Boussinesq effects to be weak and keep in all material properties only the leading-order temperature dependence beyond the Boussinesq approximation. Therefore the γ_1-term appears explicitly in (17), while in all other terms it would constitute only a quadratic correction just like the terms omitted in (8)-(11).

III. DERIVATION OF THE WEAKLY NON-BOUSSINESQ GINZBURG-LANDAU EQUATIONS

Here we derive the Ginzburg-Landau equations for weakly nonlinear hexagonal patterns in weakly non-Boussinesq convection. The main qualitative change from the Boussinesq case is that the Boussinesq symmetry, which prohibits quadratic terms in the amplitudes and therefore excludes a transcritical bifurcation to hexagons, is broken by the non-Boussinesq terms. We therefore focus on the derivation of the coefficient of the quadratic term as a function of the rotation rate and the fluid parameters. In order to obtain an asymptotically valid expansion, we assume the non-Boussinesq terms to be of the order of the convection amplitude in the nondimensionalised equations and use the expansion

$$(\vec{v},\Theta) = \delta(\vec{v_1},\Theta_1) + \delta^2(\vec{v_2},\Theta_2) + \delta^3(\vec{v_3},\Theta_3) + ..., \qquad (25)$$

$$\gamma_i = \delta\Gamma_i, \qquad i = 0..4, \qquad \delta \ll 1. \qquad (26)$$

Generally speaking, the non-Boussinesq terms lead to corrections in all coefficients of the amplitude equation. However, in the weakly non-Boussinesq case (26) only the contributions to the quadratic amplitude term and to the shift in the convection threshold appear to $\mathcal{O}(\delta^3)$ in the amplitude expansion. As mentioned before, γ_0 plays two different roles. In the buoyancy term it is the driving force for convection; it is incorporated into the Rayleigh number and is not affected by the smallness assumption (26). In the other terms it corresponds to a temperature-dependent correction of the material parameters.

We introduce the scaling

$$R = R_c(\gamma_i,\Omega) + \delta^2 R_2, \qquad T_2 = \delta^2 t, \qquad X = \delta x, \qquad Y = \delta y, \qquad (27)$$

with $R_c(\gamma_i,\Omega) = R_c(\Omega)(1+\Delta R_c(\gamma_i,\Omega))$. In this paper we mostly use the control parameter $\epsilon \equiv (R - R_c(\gamma_i,\Omega))/R_c(\gamma_i,\Omega) = \delta^2 R_2/R_c(\gamma_i,\Omega)$. The threshold shift $\Delta R_c(\gamma_i,\Omega)$, which is due to the non-Boussinesq effects, is $\mathcal{O}(\delta^2)$. We do not determine it in the weakly nonlinear expansion (26) but extract it from the Galerkin approach discussed in sec.V (see appendix for numerical values at various rotation rates). Note that we choose an isotropic scaling for the slow spatial scales rather than the anisotropic Newell-Whitehead-Segel scaling [33–35].

It follows from the continuity equation (18) that up to $\mathcal{O}(\delta^3)$ the momentum field is solenoidal,

$$\nabla \cdot \vec{v} = -\partial_t \rho = \mathcal{O}(\delta^2 \cdot \gamma_0 \cdot \delta) = \mathcal{O}(\delta^4). \tag{28}$$

Since the amplitude equation will arise from the Fredholm alternative at $\mathcal{O}(\delta^3)$, we can express the momentum in terms of poloidal and toroidal stream functions $\phi(x,y,z,t)$ and $\psi(x,y,z,t)$ [19]:

$$\vec{v} = \nabla \times \nabla \times (\vec{\mathbf{k}}\phi) + \nabla \times (\vec{\mathbf{k}}\psi) = (\partial_{xz}, \partial_{yz}, -\Delta_2)\phi + (\partial_y, -\partial_x, 0)\psi, \tag{29}$$

where $\Delta_2 = (\partial_{xx} + \partial_{yy})$. The boundary conditions for the stream functions follow from the boundary conditions (20) for the momentum $\vec{v}$:

$$\partial_{xz}\phi + \partial_y\psi = \partial_{yz}\phi - \partial_x\psi = -(\partial_{xx} + \partial_{yy})\phi = \Theta = 0 \text{ at } z = \pm\frac{1}{2}. \tag{30}$$

The evolution equations for the two stream functions are obtained by applying $\vec{\mathbf{k}} \cdot \nabla\times$ and $\vec{\mathbf{k}} \cdot \nabla \times (\nabla\times$ to (17).

Expanding the stream functions analogously to (25), the $\mathcal{O}(\delta)$-equations are given by

$$\Delta_2(\Delta^2\phi_1 - \Omega\partial_z\psi_1 - \Theta_1) = 0, \tag{31}$$

$$\Delta_2(\Omega\partial_z\phi_1 + \Delta\psi_1) = 0, \tag{32}$$

$$-R_c(\Omega)\Delta_2\phi_1 + \Delta\theta_1 = 0. \tag{33}$$

They determine the critical Rayleigh number $R_c(\Omega)$ and the critical wavenumber $q_c(\Omega)$. Since we take the non-Boussinesq terms to be of $\mathcal{O}(\delta)$, the linear problem is identical to the Boussinesq case. Thus, the critical Rayleigh number and the critical wavenumber depend only on the rotation rate Ω but not on the non-Boussinesq coefficients γ_i and one has in particular $R_c(\Omega = 0) = 1707.8$ and $q_c(\Omega = 0) = 3.12$. By introducing a suitably weighted scalar product between two functions,

$$< (\phi_1, \psi_1, \Theta_1), (\phi_2, \psi_2, \Theta_2) >= \frac{1}{V}\int dV \left(\phi_1\phi_2 + \psi_1\psi_2 + \frac{1}{R_c(\Omega)}\Theta_1\Theta_2\right), \tag{34}$$

the eigenvalue problem (31)-(33) is made self-adjoint [19].

The hexagon solution is expanded as

$$(\phi(\vec{r},t), \psi(\vec{r},t), \Theta(\vec{r},t)) = \delta\ (\phi_0(z), \psi_0(z), \Theta_0(z)) \sum_{j=1}^{3} A_j(X,Y,T_2)e^{i\vec{q}_j\cdot\vec{r}} + c.c. + \mathcal{O}(\delta^2). \tag{35}$$

Here $\vec{q}_1 = q_c\vec{n}_1$ and $\vec{q}_{2,3} = q_c\vec{n}_{2,3}$ with $\vec{n}_1 = (1,0,0)$ and $\vec{n}_{2,3} = (-1/2, \pm\sqrt{3}/2, 0)$, and $(\phi_0, \psi_0, \Theta_0)$ is the critical eigenvector of (31)-(33). Each component of the eigenvector can be expressed as a sum of three hyperbolic/trigonometric functions, respectively. We normalize the eigenvector as in [19],

$$q_c(\Omega)^2\frac{1}{V}\int dV\, \vec{v}_0 \cdot \Delta\Delta\vec{v}_0 = 1, \tag{36}$$

where $\vec{v}_0$ is the momentum associated with the stream functions ϕ_0 and ψ_0.

Due to the rotation and the presence of the non-Boussinesq terms the calculations become very involved at the higher orders in δ. For instance, at $\mathcal{O}(\delta^3)$ hundreds of products involving hyperbolic and trigonometric functions as well as powers of z are required. Thus, the final equations contain thousands of terms. To handle this, we used the analytical software package "Mathematica".

Eventually, at $\mathcal{O}(\delta^3)$ the Fredholm alternative yields the coupled Ginzburg-Landau equations for the convection amplitudes A_i,

$$\tau\partial_{T_2}A_1 = \mu A_1 + \xi^2(\vec{n}_1 \cdot \tilde{\nabla})^2 A_1 + \chi A_2^* A_3^* - \beta A_1|A_1|^2 - (\eta + \tilde{\eta})A_1|A_2|^2 - (\eta - \tilde{\eta})A_1|A_3|^2, \tag{37}$$

Cell	fluid	d [cm]	p_0 [psi]	T_0 [^oC]	$\Delta T_c^{(0)}$ [^oC]	Pr	$\gamma_0^{(0)}$	$\gamma_1^{(0)}$	$\gamma_2^{(0)}$	$\gamma_3^{(0)}$	$\gamma_4^{(0)}$	$\Omega_{1\,Hz}$
A [44]	Water	0.17	n/a	40	9.356	4.382	0.00357	0.0894	-0.167	0.0198	0.000428	54.7
B [26]	CO_2	0.052	316.18	27.3	36.04	0.865	0.181	-0.245	0.288	0.100	-0.090	4.81
C	CO_2	0.07	316.18	27.3	14.77	0.865	0.0733	-0.0965	0.118	0.0412	-0.0331	8.77

TABLE I: Parameter values for the three different cells A, B, and C used in the stability calculations (cf. eqs.(21)-(24)). The non-Boussinesq coefficients are given for a temperature difference corresponding to $R = R_c(\gamma_i = 0, \Omega = 0) = 1707.8$, which corresponds to a temperature difference $\Delta T_c^{(0)}$. The dimensionless rotation rate corresponding to $1\,Hz$ is given by $\Omega_{1\,Hz}$.

with the equations for the two remaining amplitudes obtained by cyclic permutation. Here μ is proportional to the control parameter ϵ, $\tilde{\nabla}$ is a slow gradient with respect to (X,Y), and the coherence length ξ and the relaxation time τ are related to the wavenumber dependence of the growth rate $\sigma(q)$ of the linear modes *via* $2\xi^2 = -\tau d^2\sigma/dq^2$. Note that due to the isotropic scaling there is no direct damping of transverse variations in the amplitudes. In principle, this can lead to degeneracies in certain growth rates like that of the zig-zag instability [36, 37]; to resolve these, the higher-order terms would have to be kept. For the hexagonal patterns this is, however, not necessary since there is an indirect damping; transverse variations of A_j, i.e. perpendicular to the respective $\vec{q}_j$ in (35), induce (damped) longitudinal variations of A_{j-1} and A_{j+1}, in particular through the interaction term $A^*_{j-1}A^*_{j+1}$.

The expressions for the various coefficients in (37) are much too large to be presented explicitly. Their dependence on the rotation rate and on the non-Boussinesq coefficients γ_i will be given in [38]. The Ω-dependence of the individual contributions from the various non-Boussinesq terms to the crucial quadratic coefficient χ (cf. (39) below) are shown in figs.1a,b (to be discussed below) for two realistic cases. Every effort was made to test the correctness of the coefficients. For the non-rotating non-Boussinesq case they were compared with the results for infinite Prandtl number in [19] and for arbitrary Prandtl number in [1, 39]. In both cases agreement was found except for the previously identified mistake in [19], where the contribution from γ_3 is in error for the rigid-rigid case, and for some typographic errors in [39]. For the Boussinesq case with rotation we compared our results with those in [40]. The only discrepancy we identified concerns the tricritical line of steady rolls in their fig.3. Our results are in line with [41, 42], which also indicates that the tricritical line of steady rolls in fig.3 of [40] is incorrect. This has also been discussed in [43]. Finally, we have compared our weakly nonlinear results with full numerical Galerkin solutions as discussed below (sec.V).

IV. WEAKLY NONLINEAR RESULTS

We have used the values of the coefficients of the weakly nonlinear Ginzburg-Landau equation (37) to study convection in two sample cells. Our first cell (cell A) has a thickness of $d = 0.17cm$ and is filled with water. To study convection at low Prandtl numbers, we have chosen the second cell to be a CO_2-cell of thickness $d = 0.052cm$ (cell B). Both cases correspond to cells used in previous experiments [26, 44]. The parameter values for the coefficients γ_i that we used for these cells and for an additional, thicker cell with CO_2 (cell C, discussed in more detail in sec.V) are listed in table I. As mentioned before the γ_i depend on the temperature difference applied to the cell. The values $\gamma_i^{(0)}$ listed in table I are given for a temperature difference $\Delta T_c^{(0)}$ that corresponds to $R_c(\Omega = 0, \gamma_i = 0) \equiv \alpha_0 \Delta T_c^{(0)} g d^3/\nu_0\kappa_0 = 1707.8$. Thus, within the linear approximation (21)-(24) for the temperature dependence of the fluid parameters one has the relation

$$\gamma_i(R) = \frac{R}{1707.8}\,\gamma_i^{(0)} = \frac{R_c(\Omega,\gamma_i)}{1707.8}(1+\epsilon)\,\gamma_i^{(0)}. \tag{38}$$

The second part of (38) shows that for fixed ϵ the γ_i depend on the rotation rate. Note also that to compute $R_c(\Omega, \gamma_i)$ the values of the γ_i have to be determined at ΔT_c, which in turn depends on the γ_i. This can be done iteratively and since the non-Boussinesq terms lead only to a small shift in R_c one iteration is usually sufficient. The last column in table I gives the dimensionless rotation rate $\Omega_{1\,Hz}$ that corresponds to a physical rotation rate of $1\,Hz$, which is about the typical maximal rotation rate in the experimental setups described in [26, 44].

In the spirit of [19] it is useful to identify the contributions to the quadratic coefficient χ in (37) from the

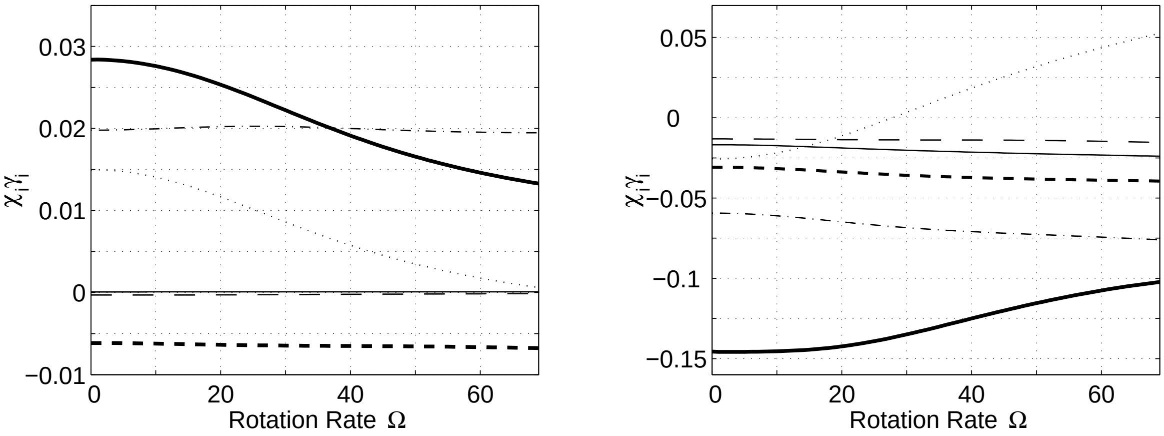

FIG. 1: Contributions to χ from the individual non-Boussinesq coefficients $\gamma_i(R_c(\Omega,\gamma_i))$ as a function of the rotation rate Ω (see equations (8)-(11) and (39)): long-dashed line - linear temperature dependence of density (γ_0), dash-dotted - quadratic temperature dependence of density (γ_1), dotted line - viscosity (γ_2), thick dashed line - heat conductivity (γ_3), thin solid line - heat capacity (γ_4). The thick solid line gives the sum χ of all non-Boussinesq effects. a) water cell A, b) CO_2-cell B.

individual non-Boussinesq terms γ_i,

$$\chi = \sum_{i=0}^{4} \chi_i(\Omega, Pr)\,\gamma_i(R_c(\Omega,\gamma_i)). \tag{39}$$

For cells A and B the dependence of χ on the rotation rate, as well as that of the individual contributions $\chi_i\,\gamma_i$ to χ from each of the non-Boussinesq coefficients γ_i, are shown in fig.1a,b. In the case of cell A (water) two contributions dominate: the quadratic density term (γ_1) and the temperature dependence of the viscosity (γ_2). In cell B these two effects are less prominent. In both cells the Ω-dependence of χ is essentially due to the viscosity term. Interestingly, in cell B its contribution even changes sign with increasing rotation rate.

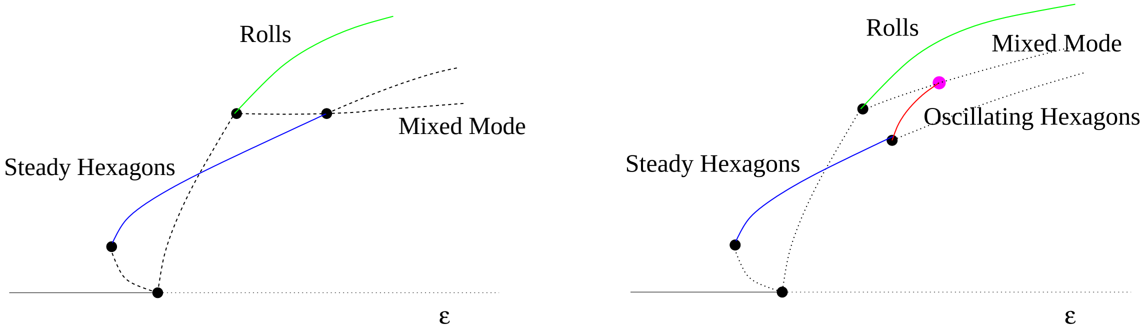

FIG. 2: Sketch of bifurcation diagrams without (a) and with (b) rotation.

In our analysis, we first focus on spatially periodic solutions at a fixed wavenumber and discuss their domains of existence and stability as a function of the rotation rate and the Rayleigh number. As sketched in the bifurcation diagram fig.2a, without rotation the steady hexagons, which arise unstably in a transcritical bifurcation from the conductive state and become stable in a saddle-node bifurcation, become unstable again in another steady transcritical bifurcation to a mixed-mode solution. Since that solution is unstable, the hexagons actually evolve to steady rolls. With rotation the secondary steady bifurcation off the hexagons turns into a Hopf bifurcation, which leads to a branch of oscillating hexagons (cf. fig.2b) [20, 21]. In the oscillating hexagons the amplitudes of the three modes making up the hexagons differ from each other and oscillate periodically with a phase shift $2\pi/3$ between them. In simulations this gives the appearance as if the centers of the convection cells were rotating.

In fig.3a,b we give the dependence of the transitions sketched in fig.2b on the rotation rate for cells A and B. Increasing the control parameter ϵ, hexagons become stable first in a saddle-node bifurcation along the thin solid line (the neutral curve is virtually indistinguishable from the saddle-node line) and are stable with respect to perturbations with the same wavevector up to the thick solid line. Rolls are only stable above the dotted line. This line diverges at a certain rotation rate Ω_{KL} beyond which rolls remain unstable for all values of ϵ. This marks the onset of the Küppers-Lortz instability [5]. More precisely, the divergence occurs for a rotation rate slightly above Ω_{KL} because the dotted line marks the stability limit of rolls within the framework of the three amplitude equations describing the hexagonal patterns. Thus, only instabilities with respect to rolls that subtend an angle of 60^o relative to the original rolls are considered. However, depending on the Prandtl number the Küppers-Lortz instability sets in at an angle somewhat below 60^o and can therefore destabilize the rolls already for lower rotation rates. The oscillating hexagons appear at the solid line and are stable up to the dashed-dotted line where they undergo a global bifurcation. In cell B (fig.3b) the non-Boussinesq effects are quite strong and the transitions occur at relatively large values of the control parameter. In this regime the weakly nonlinear approach may not be appropriate any more. We include this case mostly as an extrapolation of the weakly-nonlinear theory to the strongly nonlinear regime.

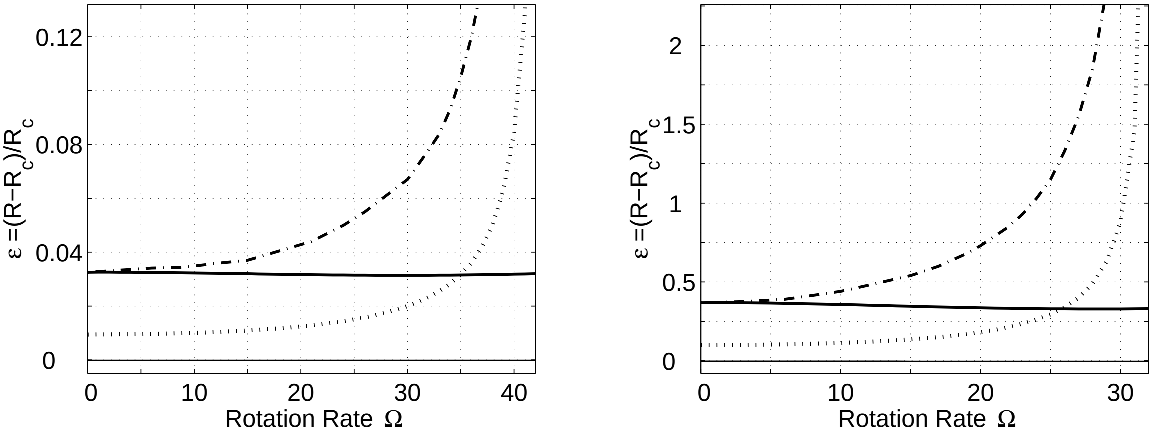

FIG. 3: Domains of existence for rolls, hexagons and oscillating hexagons for water cell A and CO_2 cell B (cf. table I). Saddle-node bifurcation of the steady hexagons (thin solid line), Hopf bifurcation of hexagons (solid line), global bifurcation to rolls (dashed-dotted line), instability of rolls (dotted).

Using the stability analysis of (37) in [14] we now give explicit stability diagrams for weakly nonlinear steady hexagons. In the absence of rotation the sideband instabilities of hexagons for both small and large Prandtl numbers are given by two longwave modes that can be described by two coupled phase equations [14, 30, 31, 45, 46]. They correspond to longitudinal and transverse deformations of the hexagon pattern, respectively. As discussed in [30, 31], both lead to the formation of defects, albeit in different configurations. While the configurations generated by the longitudinal mode heal relatively quickly, those induced by the transverse mode persist for a long time and transiently render the pattern quite disordered. The longitudinal mode becomes relevant mostly for small Prandtl numbers when mean flows are important [30]. No shortwave or oscillatory instability arises in the weakly nonlinear regime and the band of stable wavenumbers closes where it reaches the transition to the unstable mixed mode (cf. thick solid line at $\Omega = 0$ in fig.3).

Fig.4a,b gives as an example for the effect of rotation on the stability regions the weakly nonlinear results for cell A for small and intermediate rotation rates. For small rotation rates ($\Omega = 5$ in Fig.4a) the two steady long-wave phase modes persist with the transverse mode determining the stability limit for all but the smallest values of ϵ (dashed lines). For larger values of the control parameter the two modes interact and the two instability lines merge and generate an oscillatory longwave branch (dashed line above $\epsilon = 0.015$). The oscillatory part is, however, preempted by a shortwave instability (thick solid line). It is in most cases a steady instability; only if non-linear gradient terms are kept in the Ginzburg-Landau equations (37), an oscillatory shortwave instability has been found [14]. Here we do not keep, however, these higher-order terms. With increasing rotation rate the shortwave instability becomes more and more prevalent and for $\Omega = 20$ (Fig.4b), which in this cell corresponds to a rotation rate of $0.369Hz$, the stability limits are solely given by the shortwave instability. Previous simulations of (37) have shown that with rotation the long-and the shortwave instabilities typically lead to the formation of defects that eventually anneal and render a new regular hexagon pattern with different wavenumber or orientation. There are indications, however, that with nonlinear gradient terms included in (37) the defects may not always anneal, which then leads to disordered patterns with persistent chaotic dynamics [14, 32].

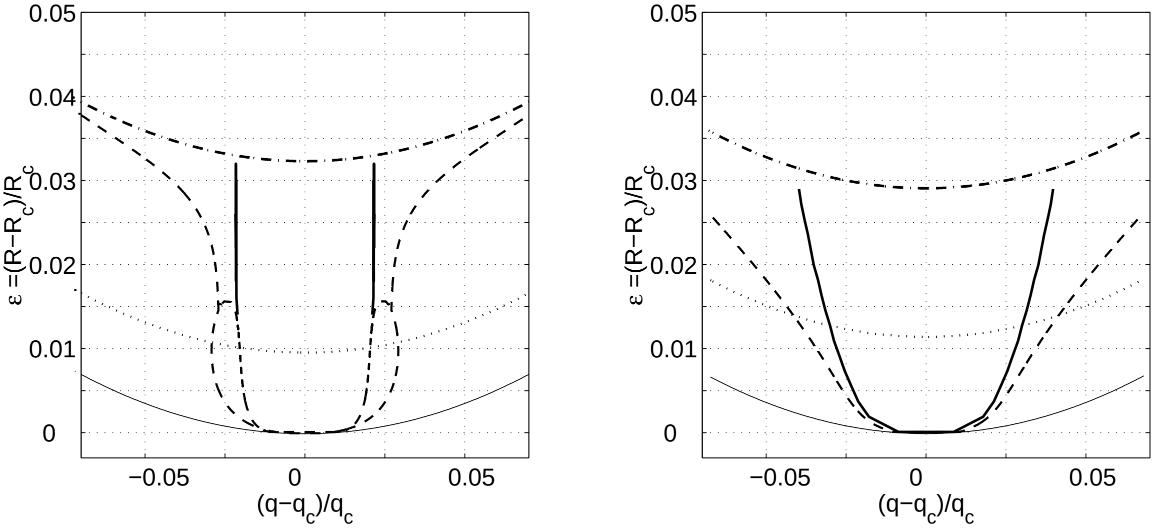

FIG. 4: Weakly nonlinear stability diagrams for steady hexagons for water cell A. a) $\Omega = 5$ ($R_c = 1721.4$, $q_c = 3.126$), b) $\Omega = 20$ ($R_c = 1898.0$, $q_c = 3.280$). Saddle-node bifurcation (thin solid line), long-wave sideband instability (dashed line), short-wave instability (thick solid line), Hopf bifurcation to oscillating hexagons (dashed-dotted line), amplitude stability limit of rolls (dotted line). In a) the long-wave instability is oscillatory above the merging of the two long-wave stability limits ($\epsilon = 0.015$). In b) it is oscillatory for all ϵ shown.

V. GALERKIN RESULTS

In this section we study the stability of hexagonal patterns in the fully nonlinear regime by solving eqs.(17)-(19) together with (20) and (21)-(24) without assuming the non-Boussinesq coefficients γ_i to be small. Thus, they are kept to all orders. In principle, also higher-order temperature derivatives of the material parameters can become important. Here we assume that the fluid properties are sufficiently well described by (8)-(11).

We compute the steady hexagon solutions using a Galerkin method on a hexagonal grid in Fourier space in the horizontal direction and an expansion in trigonometric and Chandrasekhar eigenfunctions in the vertical direction [7, 47]. The linear stability of the hexagons is then determined using a Floquet analysis, in which the Floquet parameter $\vec{p}$ is scanned over the whole Brillouin zone, adjusted for symmetries of the system. Long- and shortwave instabilities are distinguished by separate runs in which the magnitude of $\vec{p}$ is chosen in the range $(0...10^{-5})\,q_c$ and $(0.01...0.5)\,q_c$, respectively. For a complete characterization also the angle between $\vec{p}$ and the hexagon pattern as well as the eigenvector associated with the destabilizing mode of interest have to be monitored, as well. Thus, without rotation hexagon patterns have two different long-wave phase modes, a longitudinal and a transverse one, which differ in their eigenvectors. Both phase modes can destabilize the pattern [30, 31, 45, 46]. Amplitude instabilities, for which $\vec{p} = 0$, can also be relevant (cf. Hopf bifurcation to oscillating hexagons).

In the Galerkin expansion for the computation of the solution as well for its stability analysis we have typically used 4 vertical modes and have restricted the horizontal modes to those with wavenumbers up to $2q_c$. We have checked that keeping more than 4 modes in the vertical direction resulted only in a small correction in the solutions (at most 3 percent), while reducing their number below 4 could lead to changes of more than 10 percent, depending on Ω. Similarly, keeping more than 2 modes in the horizontal direction did not have any pronounced effect on the computation results for the ϵ-Ω-range considered.

To get an estimate of the expected range of validity of the weakly nonlinear analysis, we compare first the weakly nonlinear hexagon amplitudes to those obtained with the Galerkin approach. According to the weakly nonlinear theory, the convection amplitude depends on the reduced Rayleigh number ϵ as

$$A - A_{sn} \sim \sqrt{\epsilon - \epsilon_{sn}}, \tag{40}$$

where ϵ_{sn} is the reduced Rayleigh number at the saddle-node bifurcation (cf. fig.2). Fig.5a shows that for cell B the weakly nonlinear approach is limited to values of the reduced Rayleigh number up to $\epsilon \approx 0.2$.

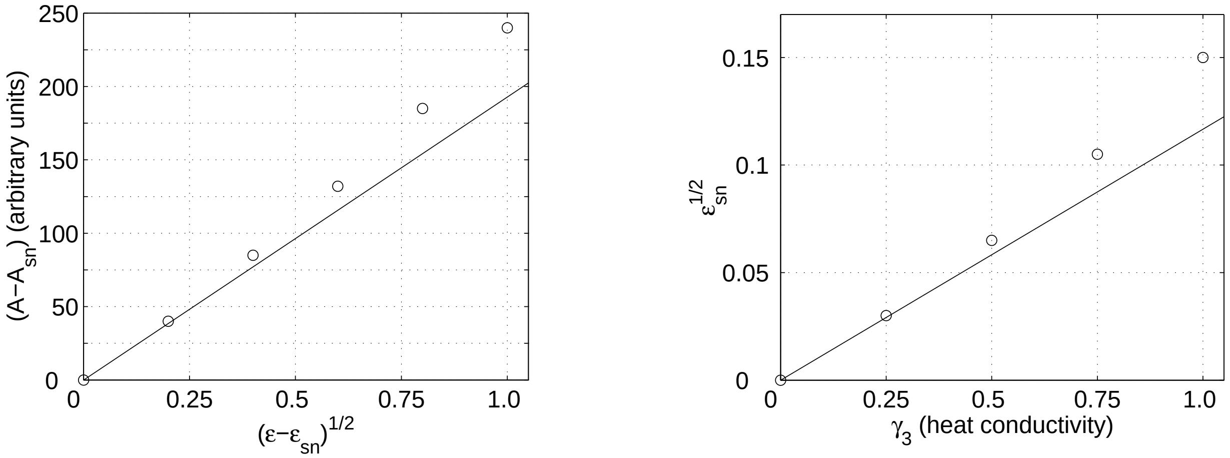

FIG. 5: Comparison of the weakly nonlinear results (solid line) with the fully nonlinear Galerkin results (symbols). a) Scaling of the convection amplitude wit ϵ. b) Location of the saddle-node bifurcation as a function of γ_3.

According to the weakly nonlinear theory $\epsilon_{sn}^{1/2}$ should be linear in the non-Boussinesq coefficients γ_i. Fig.5b shows the dependence of $\epsilon_{sn}^{1/2}$ on γ_3, the non-Boussinesq term associated with the heat conductivity. It exhibits the strongest nonlinearity of all γ_i. This criterion suggests that the weakly nonlinear, weakly non-Boussinesq approach (26), in which the contributions of the non-Boussinesq effects to the cubic coefficients and the nonlinear contributions to the quadratic terms in (37) are omitted, is limited to values $\gamma_i < 0.5$.

We now present stability regimes for the three different cells listed in table I covering moderate and low Prandtl numbers. First, we consider the system with moderate Prandtl number (water cell A). Fig.6 shows the stability limits for hexagons and rolls without and with rotation. In order to compare with the weakly nonlinear analysis we have chosen a relatively thick cell for which the non-Boussinesq effects and consequently the hexagon amplitudes are quite small. Thus, the instability of the hexagons to rolls occurs at a value of ϵ as low as 0.04 (dashed-dotted line). In the absence of rotation, $\Omega = 0$, all sideband instabilities of the hexagons are longwave instabilities (dashed line in Fig.6a). Rolls are linearly stable all the way down to $\epsilon \approx 0.01$ depending on their wavenumber (dotted line). In the order of increasing wavenumber (from left to right), the three segments of their stability limits are given by the zig-zag instability involving long-wave modulations along the roll axis, the amplitude instability to hexagons, and the knot instability towards square patterns, respectively.

Fig.6b shows the stability limits with relatively slow rotation ($\Omega = 5$, which corresponds to $0.0923 Hz$). Compared to the non-rotating case, the two longwave instabilities of the hexagons merge now at $\epsilon \approx 0.010$ for $q < q_c$ and at $\epsilon \approx 0.013$ for $q > q_c$. Above these values they become oscillatory (cf. fig.4a). However, as in the weakly nonlinear approach this oscillatory branch is preempted by a shortwave instability (solid line). For a comparison, the open circles give the stability limits obtained in the weakly nonlinear approach. Very close to onset the two limits agree well. For larger ϵ, however, deviations arise. Most notably, the numerical stability limits develop a clear asymmetry in $q - q_c$. It may be due to higher-order nonlinear gradient terms (cf. [14, 46]) or due to finite Prandtl number effects, which lead to the excitation of a (weak) mean flow (cf. [30]). Both effects act differently for larger and smaller wavenumbers and are not contained in the leading-order Ginzburg-Landau equation (37). The diamonds denote the parts of the stability limits along which the instability is oscillatory, i.e. for which the imaginary part of the leading eigenvalue with positive real part is larger than 10^{-4}. Along the dashed-dotted line with solid diamonds the oscillatory instability is an amplitude instability. There the oscillating hexagons bifurcate off the steady hexagons (see also figs.2b,3a) [14, 20, 21]. Close to that transition the shortwave instability of the steady hexagons also becomes oscillatory on the low-q side.

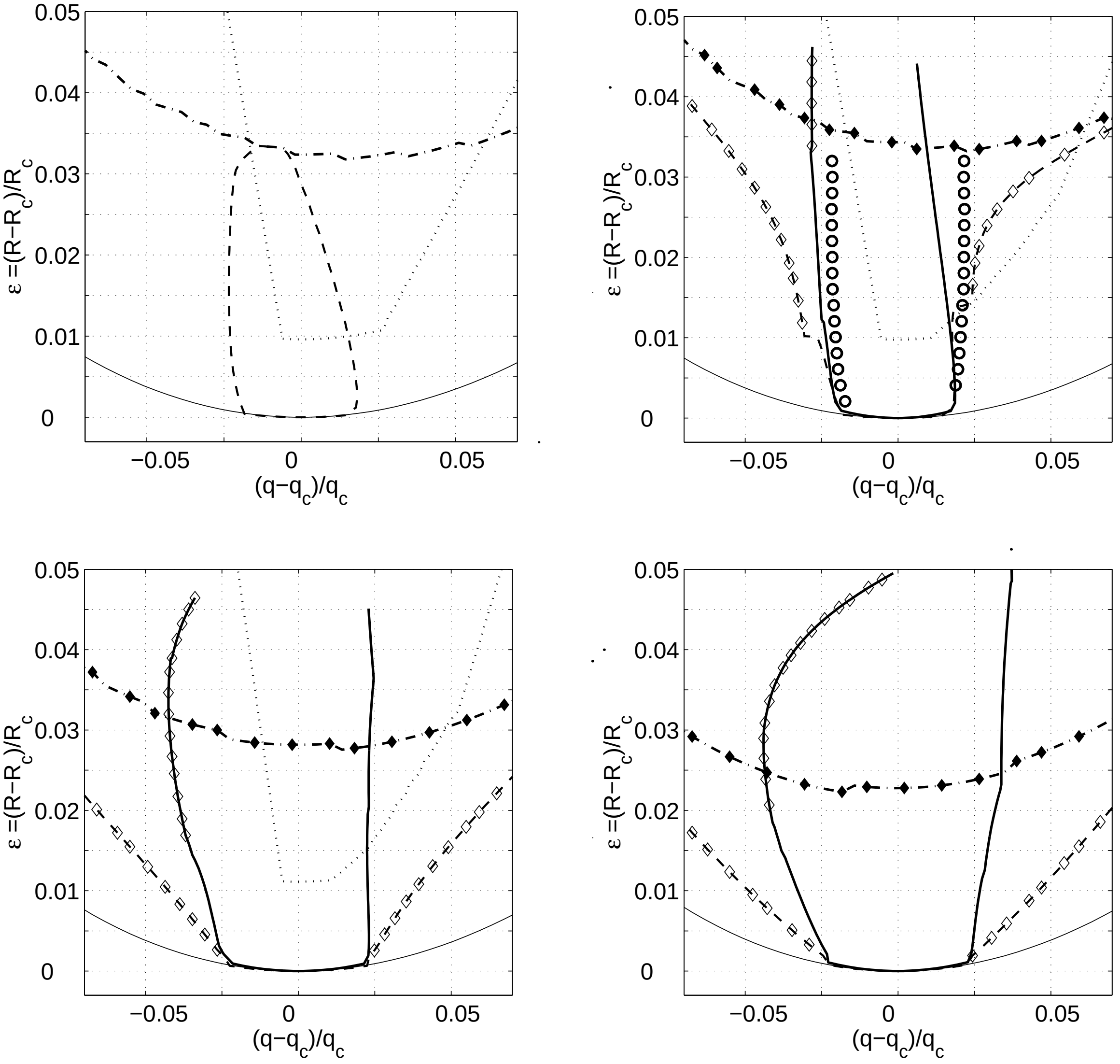

FIG. 6: Stability limits of steady hexagons for cell A with increasing Ω. a) $\Omega = 0$ ($R_c = 1705.9$, $q_c = 3.114$), b) $\Omega = 5$ ($R_c = 1718.2$, $q_c = 3.126$), c) $\Omega = 20$ ($R_c = 1859.3$, $q_c = 3.280$), d) $\Omega = 40$ ($R_c = 2389.4$, $q_c = 3.650$). Saddle-node bifurcation (thin solid line), long-wave instability (dashed line), short-wave instability (thick solid line), Hopf bifurcation to oscillating hexagons (solid diamonds), stability limits of rolls (dotted line). Open diamonds indicate oscillatory side-band instabilities. In a) the dashed-dotted line indicates the amplitude instability of hexagons to the mixed-mode. In b) the open circles give the stability limits obtained from the weakly nonlinear analysis.

With increasing rotation rate the steady longwave instabilities are confined to a decreasing range in ϵ and eventually disappear as shown in fig.6c,d ($\Omega = 20$ and $\Omega = 40$). Consequently, the short-wave instability sets in essentially immediately above threshold; the ϵ-range over which it is oscillatory increases, as well. At the same time the stability limit of rolls is shifted to larger values of ϵ. For $\Omega = 40$ they become linearly stable only for values of ϵ well above the transition from steady to oscillatory hexagons (Fig.6d).

Now we turn to fluids with low Prandtl number and show in fig.7 the stability limits for cell B, which exhibits strong non-Boussinesq effects. Even in the absence of rotation (fig.7a) the stability limits for the steady hexagons are strongly asymmetric in $q - q_c$ and resemble qualitatively those obtained in a weakly nonlinear approach that includes the effects of mean flow [30]. In particular, the dramatic change in behavior at very small ϵ on the high-q side is noteworthy in this respect. Along that stability limit it is difficult to determine whether the instability is long- or shortwave since modes with small and large values of the Floquet parameter $\vec{p}$ become unstable within a very narrow window of parameters.

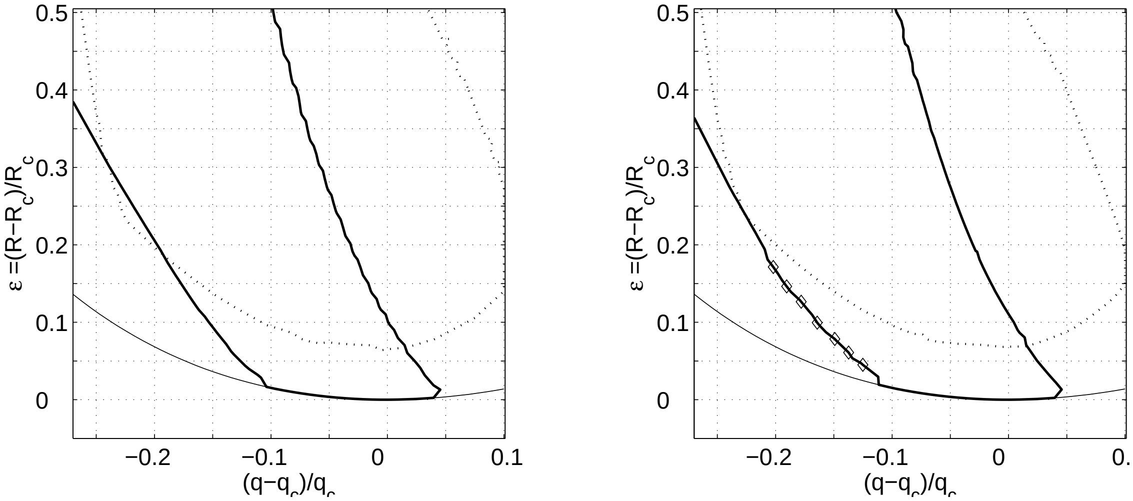

FIG. 7: Stability limits for hexagons and rolls for CO_2-cell B. a) $\Omega = 0$ ($R_c = 1687.3$, $q_c = 3.118$), b) $\Omega = 4.612$, corresponding to 1 Hz ($R_c = 1697.8$, $q_c = 3.127$). Saddle-node bifurcation (thin solid line), side-band instability (thick solid line), stability limits of rolls (dotted line). Diamonds indicate oscillatory instability.

It is remarkable that the hexagons remain amplitude-stable with respect to the mixed mode (cf. fig.2) up to quite large values of ϵ. In fact, in our computations, which covered the range up to $\epsilon = 0.5$ and higher, we did not encounter the amplitude instability at all. This may be related to the fact that the non-Boussinesq effects γ_i become stronger with increasing ϵ, i.e. with increasing ΔT (cf. (38)). Thus, at least for idealized periodic boundary conditions no transition from hexagons to rolls is expected to occur up to $\epsilon = 0.5$. Rolls, on the other hand, are linearly stable down to $\epsilon = 0.1$, yielding nominally a large hysteresis between the hexagons and the rolls. One may surmise that even in experimental set-ups in which rolls are present at the side walls the rolls will invade the hexagonal patterns only for ϵ-values well above 0.1. However, in experiments a transition from hexagons to rolls has been reported already for ϵ-values as low as 0.1 [26]. The stability results of fig.7a suggest that this transition is actually not that associated with the amplitude instability of hexagons to the mixed mode but with a sideband instability, which then triggers a transition to the rolls *via* the nucleation of defects.

In the case of rotation (fig.7b) the absence of the amplitude instability to the mixed mode all the way to $\epsilon = 0.5$ implies that in this range of ϵ also no Hopf bifurcation to oscillating hexagons occurs. The side-band stability limits of the steady hexagons are hardly affected by the rotation on the high-q side. However, on the low-q side the sideband instability becomes oscillatory, with frequencies ranging from 0.1 to 0.4.

An interesting aspect of this strongly non-Boussinesq case is that for the larger Rayleigh numbers spatial resonances between modes of different wavenumbers come into play near the left stability limit of the hexagons. The first such resonance involves the modes A_i with the fundamental wavevectors $q\vec{n}_i$ and their harmonics B_i with wavevectors $q\,(\vec{n}_i - \vec{n}_{i+1})$. The latter modes are rotated by 30^o relative to the fundamental modes. As the wavenumber q of the hexagons is decreased the harmonic modes B_i become dominant and the fundamental modes A_i go to 0 already before the neutral curve is reached. Thus, the solution branch corresponding to the usual hexagons ends on a branch of hexagons with larger wavenumber. This bifurcation influences the stability limits of the hexagons [48].

One of the goals of the current work is to explore whether the regime of oscillating hexagons can be reached experimentally. There is always a competition with the roll states, and one may speculate that the situation is most favorable if the roll states are Küppers-Lortz unstable, which requires relatively large dimensionless rotation rates Ω. For fixed physical rotation rate the dimensionless rotation rate Ω increases with increasing layer thickness. However, for a given fluid, the non-Boussinesq effects decrease with increasing thickness, and, as a consequence, the ϵ-range for the oscillating hexagons is shifted to smaller and smaller values of ϵ where they are difficult to study experimentally. Thus, for a given maximal physical rotation rate and a given fluid the maximal dimensionless rotation rate is obtained when the thickness is chosen such that the oscillating hexagons arise at values of ϵ near the experimental resolution.

As shown in Fig.6d, in cell A (water) the lower stability limit of rolls is shifted above the onset of the

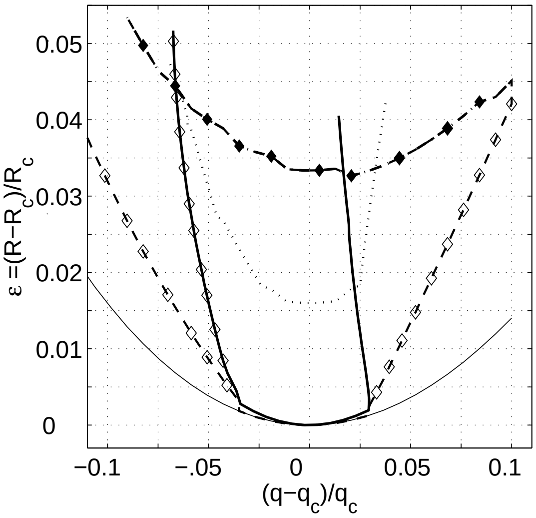

FIG. 8: Stability limits for hexagons and rolls for cell C at $\Omega = 8.77$, corresponding to $1Hz$; $R_c = 1743.1$, $q_c = 3.149$. Saddle-node bifurcation (thin solid line), side-band instability (thick solid line), Hopf bifurcation to oscillating hexagons (solid diamonds), stability limits of rolls (dotted line). Diamonds indicate oscillatory instability.

oscillating hexagons already for a rotation rate of $0.73Hz$. In cell B, containing CO_2, no transition to oscillating hexagons was found up to $\epsilon = 0.5$ and higher. We therefore investigate another cell at low Prandtl number (CO_2-cell C), which is thicker, and show in fig.8 the corresponding stability results. For the chosen thickness the oscillating hexagons appear at a value of ϵ that is close to the resolution limit at which minute experimental cell inhomogeneities come into play. A physical rotation rate of $1Hz$ then yields $\Omega = 8.77$. For this rotation rate the long-wave instability is oscillatory over the whole range of ϵ. The relevant side-band instabilities are, however, short-wave. They are steady on the large-q side and oscillatory on the low-q side. In contrast to the thinner CO_2-cell, this cell exhibits a transition to oscillating hexagons. For this rotation rate it is, however, still above the lower stability limit of rolls and bistability between the oscillating hexagons and rolls exists.

VI. CONCLUSION

In this paper we have investigated the stability of hexagon patterns in rotating non-Boussinesq convection with an emphasis on quantitative results for specific, experimentally relevant configurations. This work complements previous analyses of coupled Ginzburg-Landau equations in the weakly nonlinear regime and of Swift-Hohenberg-type equations. While previously the focus was on the qualitative features that can be expected in hexagon patterns with broken chiral symmetry [14–18, 30] here we have determined the coefficients in the Ginzburg-Landau equations and their dependence on the fluid and system parameters. For the strongly nonlinear regime we have utilized a Galerkin method.

The weakly nonlinear analysis, which focused on moderate Prandtl numbers (using water as the fluid), confirmed the expected transition from longwave to shortwave steady sideband perturbations as the instabilities that limit the band of stable wavenumbers. In this regime the oscillatory instability that arises from the interaction of the two different phase modes is experimentally not relevant. This analysis also gives the existence range of the oscillating hexagons that arise in a Hopf bifurcation off the steady hexagons and end in a heteroclinic cycle as the Rayleigh number is increased.

The fully nonlinear Galerkin analysis confirmed the validity of the leading-order weakly nonlinear results close to threshold and for not too small Prandtl numbers. For small Prandtl numbers, as exemplified by CO_2 as fluid, the stability region becomes very asymmetric indicating the relevance of higher-order gradient terms or of a mean flow driven by pattern deformations. Similar stability regions have been obtained in a weakly nonlinear analysis in which the three coupled Ginzburg-Landau equations are extended to include the non-local interaction induced by the mean flow [30]. A comparison with that analysis suggests that the longwave modes that limit the stable band of wavenumbers in the non-rotating system are different on the high- and the low-wavenumber side. For large wavenumbers the destabilizing mode is expected to be the transverse phase mode, whereas for low wavenumbers the longitudinal mode is predicted. It was found that the transverse mode leads to much more disordered transient patterns and as a consequence the ensuing relaxation to the stable pattern takes noticeably longer [30]. Once the system is rotated, the relevant perturbations on the low-wavenumber side become oscillatory. The nonlinear evolution developing from this instability is not known.

Interestingly, in the strongly non-Boussinesq case, which in fact corresponds to the experimental set-up of [26], no amplitude instability from steady hexagons to rolls *via* the mixed mode could be found for $\epsilon < 0.5$. Experimentally, however, in the absence of rotation the transition from hexagons to rolls had been observed near $\epsilon = 0.1$. Based on our stability analysis this transition would be expected to be a sideband instability of hexagons rather than the amplitude instability associated with the mixed mode, suggesting that the transition to rolls would involve the formation of defects from which then rolls invade the hexagon patterns. The fact that in the experiments rolls are always present to some extent near the boundaries may make the interpretation of the transition more subtle.

In the strongly non-Boussinesq case, in which the hexagons are linearly stable quite far above onset, the hexagon solutions with small wavenumbers are strongly influenced by a spatial resonance involving the fundamental modes and their first harmonics, similar to the case of Taylor vortex flow [49–51]. While in the latter case the pattern is quasi-onedimensional and the resonating wavenumbers have a ratio of $1:2$, the resonance of the two-dimensional hexagon patterns involves modes subtending an angle of 30^o and with wavenumber ratio $1:\sqrt{3}$. Similar to the case of Taylor vortex flow, the solution branch of the usual (hexagon) pattern ends on the branch of harmonic modes. This bifurcation occurs very close to the side-band stability limit of the hexagons [48].

We have also determined the stability regions of roll convection in these non-Boussinesq cases without and with rotation. For the high-Prandtl number case rotation rates are experimentally accessible at which the rolls become linearly stable only above the transition from steady to oscillating hexagons. One may expect that this would provide a situation in which oscillating hexagons are experimentally accessible. It is, however, possible that the instability of the rolls does not lead to the linearly stable oscillating hexagons, which are the only spatially periodic stable solutions, but instead to a disordered chaotic state of the Küppers-Lortz type.

We have not addressed the stability of hexagons that have slightly different wavevectors in the three components [52].

The predictions for the stability boundaries and the type of instabilities determining them appear now amenable not only to numerical simulations but also to experimental studies since recently the printing of two-dimensional convection patterns by laser heating has been used successfully in measuring the band of stable wavenumbers in hexagonal Marangoni convection [24]. In particular the oscillatory sideband instability identified in our stability analysis may lead to interesting dynamics.

We are very grateful to G. Ahlers for providing us with a program to determine the properties of water and CO_2 in the different experimental regimes.

This work was supported by the Engineering Research Program of the Office of Basic Energy Sciences at the Department of Energy (DE-FG02-92ER14303), by a grant from NASA (NAG3-2113), by a grant from NSF (DMS-9804673) and by one author's (V.M.) wife Yelena Ledneva.

VII. APPENDIX

The non-Boussinesq terms γ_i lead to shifts ΔR_c and Δq_c in the threshold value of the Rayleigh number and the associated critical wavenumber, respectively. To leading order in γ_i the shifts are quadratic in the non-Boussinesq terms,

$$R_c(\gamma_i,\Omega) = R_c(0,\Omega)\left(1+\sum_{i,j=0}^{4}\Delta R_{ij}(\Omega)\,\gamma_i\gamma_j\right), \tag{41}$$

$$q_c(\gamma_i,\Omega) = q_c(0,\Omega)\left(1+\sum_{i,j=0}^{4}\Delta q_{ij}(\Omega)\,\gamma_i\gamma_j\right). \tag{42}$$

Note that in (41,42) the γ_i are given by those corresponding to $R_c(0,\Omega)$ (cf. (38)). In principle, due to the dependence of the γ_i on the temperature difference, which in turn depends on the Rayleigh number, the critical Rayleigh number is given by a nonlinear eigenvalue problem, which can be solved iteratively. However, since the threshold shift due to the non-Boussinesq terms is quite small for most experimental situations, the leading-order correction of $\mathcal{O}(\gamma_i^2)$ indicated in (41,42) with γ_i corresponding to $R_c(\gamma_i = 0, \Omega)$ is sufficient. In tables II,III,IV we give the coefficients ΔR_{ij} and Δq_{ij} for $\Omega = 0$, $\Omega = 30$, and $\Omega = 50$, respectively. Since the coefficient matrices ΔR_{ij} and Δq_{ij} are symmetric the upper right triangle of each table gives the coefficients Δq_{ij} for $i = 0..4$ and $j = i..4$, whereas the lower left triangle gives the coefficients ΔR_{ij}, for $i = 0..4$ and $j = 0..i$. Note that in the sums in (41,42) the off-diagonal terms are summed over twice. It is worth noting that some of the coefficients depend non-monotonically on Ω over the range $\Omega = 0$ to $\Omega = 50$, e.g. ΔR_{00} increases and decreases substantially over that range of Ω.

			0	1	2	3	4	$10^3 \cdot \Delta q_{ij}$
0	0.597		-1.336	0.464	-0.000	-0.000	-0.231	0
1	-0.367	-0.758		-3.318	2.633	5.422	-3.653	1
2	0.000	2.233	-5.074		4.821	-2.636	1.316	2
3	0.000	4.499	-2.232	-4.521		-5.432	2.665	3
4	0.183	-1.514	1.116	0.948	-0.189		-0.831	4
$10^2 \cdot \Delta R_{ij}$	0	1	2	3	4			

TABLE II: Expansion coefficients $\Delta R_{ij}(\times 10^2)$ and $\Delta q_{ij}(\times 10^3)$ for the threshold shift and the shift in the critical wavenumber, respectively, for $\Omega = 0$.

			0	1	2	3	4	$10^3 \cdot \Delta q_{ij}$
0	-0.247		2.968	-0.938	0.002	-0.000	0.469	0
1	-0.069	-1.431		-5.160	4.055	6.800	-4.509	1
2	-0.000	1.966	0.763		-15.90	-4.064	2.028	2
3	0.000	5.668	-1.970	-5.700		-6.793	3.553	3
4	0.034	-2.174	0.983	1.449	-0.357		-1.289	4
$10^2 \cdot \Delta R_{ij}$	0	1	2	3	4			

TABLE III: Expansion coefficients $\Delta R_{ij}(\times 10^2)$ and $\Delta q_{ij}(\times 10^3)$ for the threshold shift and the shift in the critical wavenumber, respectively, for $\Omega = 30$.

			0	1	2	3	4	$10^3 \cdot \Delta q_{ij}$
0	-0.229		1.837	-1.315	0.000	-0.001	0.659	0
1	0.036	-2.053		-6.955	5.290	7.985	-5.274	1
2	-0.000	1.629	2.752		-17.97	-5.302	2.646	2
3	-0.000	6.715	-1.638	-6.758		-7.952	4.385	3
4	-0.018	-2.743	0.815	1.892	-0.513		-1.739	4
$10^2 \cdot \Delta R_{ij}$	0	1	2	3	4			

TABLE IV: Expansion coefficients $\Delta R_{ij}(\times 10^2)$ and $\Delta q_{ij}(\times 10^3)$ for the threshold shift and the shift in the critical wavenumber, respectively, for $\Omega = 50$.

---

[1] E. Bodenschatz, W. Pesch, and G. Ahlers, Ann. Rev. Fluid Mech. **32**, 709 (2000).
[2] F. Busse and K. Heikes, Science **208**, 173 (1980).
[3] Y. Hu, R. Ecke, and G. Ahlers, Phys. Rev. E **55**, 6928 (1997).
[4] Y. Hu, W. Pesch, G. Ahlers, and R. E. Ecke, Phys. Rev. E **58**, 5821 (1998).
[5] G. Küppers and D. Lortz, J. Fluid Mech. **35**, 609 (1969).
[6] S. Morris, E. Bodenschatz, D. Cannell, and G. Ahlers, Phys. Rev. Lett. **71**, 2026 (1993).
[7] W. Decker, W. Pesch, and A. Weber, Phys. Rev. Lett. **73**, 648 (1994).
[8] Y. Hu, R. Ecke, and G. Ahlers, Phys. Rev. Lett. **74**, 391 (1995).
[9] S. W. Morris, E. Bodenschatz, D. S. Cannell, and G. Ahlers, Physica D **97**, 164 (1996).
[10] K. M. Bajaj, D. S. Cannell, and G. Ahlers, Phys. Rev. E **55**, R4869 (1997).
[11] D. A. Egolf, I. V. Melnikov, W. Pesch, and R. E. Ecke, Nature **404**, 733 (2000).
[12] Q. Ouyang and H. Swinney, Chaos **1**, 411 (1991).
[13] K. Eckert, M. Bestehorn, and A. Thess, J. Fluid Mech. **356**, 155 (1998).
[14] B. Echebarria and H. Riecke, Physica D **139**, 97 (2000).
[15] B. Echebarria and H. Riecke, Phys. Rev. Lett. **84**, 4838 (2000).
[16] B. Echebarria and H. Riecke, Physica D **143**, 187 (2000).
[17] F. Sain and H. Riecke, Physica D **144**, 124 (2000).
[18] A. M. Mancho and H. Riecke, Chaos (submitted).
[19] F. H. Busse, J. Fluid Mech. **30**, 625 (1967).
[20] J. Swift, in *Contemporary Mathematics Vol. 28* (American Mathematical Society, Providence, 1984), p. 435.
[21] A. Soward, Physica D **14**, 227 (1985).
[22] H. Chaté and P. Manneville, Physica A **224**, 348 (1996).
[23] K. Nitschke and A. Thess, Phys. Rev. E **52**, 5772 (1995).
[24] D. Semwogerere and M. F. Schatz, Phys. Rev. Lett. **88**, 054501 (2002).
[25] S. Ciliberto, E. Pampaloni, and C. Perez-Garcia, Phys. Rev. Lett. **61**, 1198 (1988).
[26] E. Bodenschatz, J. R. deBruyn, G. Ahlers, and D. Cannell, Phys. Rev. Lett. **67**, 3078 (1991).
[27] E. Siggia and A. Zippelius, Phys. Rev. Lett. **47**, 835 (1981).
[28] W. Decker and W. Pesch, J. Phys II (Paris) **4**, 419 (1994).
[29] A. Bernoff, Euro. J. Appl. Math. **5**, 267 (1994).
[30] Y. Young and H. Riecke, Physica D **163**, 166 (2002).
[31] M. Sushchik and L. Tsimring, Physica D **74**, 90 (1994).
[32] Y. N. Young and H. Riecke, in preparation .
[33] A. Newell and J. Whitehead, J. Fluid Mech. **38**, 279 (1969).
[34] L. Segel, J. Fluid Mech. **38**, 203 (1969).
[35] G. Gunaratne, Q. Ouyang, and H. Swinney, Phys. Rev. E **50**, 2802 (1994).
[36] T. Callahan and E. Knobloch, Phys. Rev. E **64**, 036214 (2001).
[37] B. Echebarria and H. Riecke, Physica D **158**, 45 (2001).
[38] V. Moroz, Ph.D. thesis, Northwestern University, in preparation.
[39] A. Tschammer, Ph.D. thesis, Universität Bayreuth, 1996.
[40] T. Clune and E. Knobloch, Phys. Rev. E **47**, 2536 (1993).
[41] F. H. Busse and J. A. Whitehead, J. Fluid Mech. **47**, 305 (1971).
[42] R. M. Clever and F. Busse, J. Fluid Mech. **94**, 609 (1979).
[43] K. M. Bajaj, G. Ahlers, and W. Pesch, Phys. Rev. E **65**, 056309 (2002).
[44] K. Bajaj, J. Liu, B. Naberhuis, and G. Ahlers, Phys. Rev. Lett. **81**, 806 (1998).
[45] J. Lauzeral, S. Metens, and D. Walgraef, Europhys. Lett. **24**, 707 (1993).
[46] B. Echebarria and C. Pérez-García, Europhys. Lett. **43**, 35 (1998).
[47] R. M. Clever and F. H. Busse, J. Fluid Mech. **65**, 625 (1974).
[48] V. Moroz and H. Riecke, in preparation .
[49] M. Dominguez-Lerma, D. Cannell, and G. Ahlers, Phys. Rev. A **34**, 4956 (1986).
[50] H. Riecke and H.-G. Paap, Phys. Rev. A **33**, 547 (1986).
[51] H. Paap and H. Riecke, Phys. Rev. A **41**, 1943 (1990).
[52] A. E. Nuz, A. A. Nepomnyashchy, and L. M. Pismen, Physica A **249**, 179 (1998).